Ultramicroscopy 254 (2023) 113833

Contents lists available at ScienceDirect

Ultramicroscopy

journal homepage: www.elsevier.com/locate/ultramic

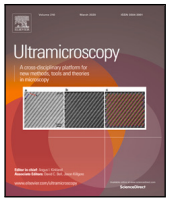

Scanning capacitance microscopy of GaN-based high electron mobility transistor structures: A practical guide

Chen Chen [a,*], Saptarsi Ghosh [a], Francesca Adams [a], Menno J. Kappers [a], David J. Wallis [a,b], Rachel A. Oliver [a]

[a] Department of Materials Science and Metallurgy, University of Cambridge, Cambridge CB3 0FS, United Kingdom
[b] Centre for High Frequency Engineering, University of Cardiff, Cardiff CF24 3AA, United kingdom

ARTICLE INFO

Dataset link: https://doi.org/10.17863/CAM.100633

Keywords:
Scanning capacitance microscopy
High electron mobility transistor structures
Plan-view characterisation

ABSTRACT

The scanning capacitance microscope (SCM) is a powerful tool to characterise local electrical properties in GaN-based high electron mobility transistor (HEMT) structures with nanoscale resolution. We investigated the experimental setup and the imaging conditions to optimise the SCM contrast. As to the experimental setup, we show that the desired tip should be sharp (e.g., with the tip radius of ≤ 25 nm) and its coating should be made of conductive doped diamond. Most importantly, its spring constant should be large to achieve stable tip-sample contact. The selected tip should be positioned close to both the edge and Ohmic contact of the sample. Regarding the imaging conditions, we also show that a dc bias should be applied in addition to an ac bias because the latter alone is not sufficient to deplete the two-dimensional electron gas (2DEG) in the AlGaN/GaN heterostructure. The approximate range of the effective dc bias values was found by measuring the local dC/dV-V curves, yielding, after further optimisation, two optimised dc bias values which provide strong, but opposite, SCM contrast. In comparison, the selected ac bias value has no significant impact on the SCM contrast. The described methodology could potentially also be applied to other types of HEMT structures, and highly-doped samples.

1. Introduction

Scanning capacitance microscopy (SCM) is an atomic force microscopy (AFM)-based technique. It can be used to characterise the carrier density and type near the surface of semiconductor materials [1]. Numerous studies have used SCM to study different semiconductor materials such as Si [2,3], Ge [4], GeSi [5,6], InAs [7], GaAs [8], GaN [9,10] etc, and different structures such as quantum dots [7], nanowires [11,12], quantum wells [13], etc. Our interest lies with the group-III nitrides, being an important semiconductor for electronic [14–17] and optical [18–21] devices. SCM studies of GaN bulk materials have been done in both plan-view [9,10] and cross-sectional [10] geometries. Typically, plan-view studies are conducted on the as-grown surface of a sample while cross-sectional studies are conducted on cleaved surfaces. For example, Hansen et al. [9] made a plan-view SCM study of the relationship between dislocation-related surface pits and the near-surface electrical properties of GaN films grown on *c*-plane sapphire. Recently, Minj et al. [22] studied III-N heterostructures in cross-section. By combining SCM data with conductive-atomic force microscopy (C-AFM) data, they revealed the nature of free carriers originating from extrinsic n-type and p-type dopants and showed the existence of polarisation induced confined carriers, providing evidence for both a two-dimensional electron gas and significantly a two-dimensional hole gas.

GaN-based high electron mobility transistors (HEMTs) are promising for high power switching applications [14,16] and RF applications [15]. Choi et al. [23] conducted a cross-sectional SCM study of GaN-based HEMT structures grown on Si(111), with a focus on the electrical properties in the buffer layer. There are also plan-view studies of GaN-based HEMT structures to investigate the electrical properties in the two-dimensional electron gas (2DEG) layer near the surface, which is of significant importance. The large lattice mismatch between GaN and commonly used substrates such as sapphire, SiC, and Si typically leads to a large density of threading dislocations (TDs) in epitaxial device layers [24]. In the case of Si substrates [25,26], TDs with a typical density of $\sim 10^9\,\mathrm{cm}^{-2}$ propagate through the 2DEG and terminate at the surface, forming surface defects such as pits [27]. These surface defects may result in device reliability challenges such as device breakdown [28,29], current collapse [30,31], etc. Additionally, the inhomogeneity of the AlGaN barrier layer in terms of layer thickness and composition may also cause local variation in the electrical

* Corresponding author.
E-mail address: cc2053@cam.ac.uk (C. Chen).

https://doi.org/10.1016/j.ultramic.2023.113833
Received 2 December 2022; Received in revised form 12 July 2023; Accepted 17 August 2023
Available online 22 August 2023

properties of the 2DEG [32,33]. For example, Smith et al. investigated local lateral variations in AlGaN barrier layer thickness [32], negatively charged threading edge dislocations [33], and charging effects [34]. These above examples indicate that SCM is a promising tool to study the impact of the surface defects and barrier layer inhomogeneity on the local electrical properties of HEMTs with micron- to nanoscale resolution.

The optimisation of SCM characterisation for chemically doped samples has been widely reported [35–38]. However, its optimisation for polarisation-induced doping has not been reported, making the collection of reliable data difficult. Here, as an example of a polarisation-doped sample, we address the optimisation of SCM for GaN-based HEMTs in plan view. Although previously reported plan view SCM images of HEMTs [32–34] are, as we have noted above, indicative of the promise of the technique in this context, the contrast which has been achieved in these studies is generally weak and only at a micron-scale resolution, suggesting that further optimisation is necessary. We suggest that it should be possible to achieve resolution in SCM of HEMTs of the order of tens of nanometers, although this will be fundamentally limited by either the size of the tip or the thickness of the barrier, whichever is the larger of the two.

Therefore, to reach the full potential of the SCM technique for the plan-view characterisation of GaN-based HEMT heterostructures, we focus here on investigating the impact of the experimental setup and imaging conditions on the SCM contrast. To aid the SCM setup optimisation process, the selected sample is a HEMT structure of which the surface exhibits a low density of fissure formation. Surface fissures in AlGaN/GaN structures have been found to compromise the integrity of the 2DEG [39]. Our preliminary observations showed that the fissures indeed cause local variations of the SCM contrast. Hence, this study should be seen firstly as a practical guide for plan-view SCM analysis of HEMT structures in particular and secondly as a contribution towards the development of a solid basis for studies into the relationship between surface defect structure, sub-surface layer inhomogeneity, and near-surface electrical properties of semiconductor structures in general.

2. Scanning capacitance microscopy

2.1. Working principle

In SCM, a conductive tip scans over a semiconductor surface in contact mode [40]. If the semiconductor surface has a natural oxide layer, a metal–oxide–semiconductor (MOS) capacitor will be formed by the conductive tip, the oxide layer, and the semiconductor [40]. SCM also works reasonably well even without an oxide layer on the semiconductor surface as long as the tip-sample contact forms a Schottky barrier [41]. In either case, a high-frequency ac bias is applied to the tip to induce capacitance changes which occur in a doped layer due to either the accumulation or the depletion of mobile carriers in the near-surface region [Fig. 1(a)] [1]. For a change in bias of fixed amplitude (ΔV), the local carrier density will determine the change in local capacitance (ΔC) [1]. Surface regions with lower local carrier density can be more easily depleted, hence ΔC is bigger. As a result, the slope of the local *C-V* curve is steeper. In SCM, a change in bias (ΔV) is achieved via the application of an ac bias, and the output signal is the dC/dV amplitude, which is larger for lower local carrier densities. Hence, a map of the *dC/dV* amplitude signal can indicate the distribution of local carrier density.

In semiconductors with high carrier density, the *dC/dV* amplitude signal can be weak or even hardly detectable because standard SCM setups apply insufficient ac bias to achieve depletion. However, the effective depletion of carriers is a prerequisite for SCM characterisation because sufficient capacitance change is needed.

The sign of the *C-V* curve slope, given by the *dC/dV* phase signal, can indicate n-type or p-type material [40]. Surface topography, *dC/dV* amplitude map, and *dC/dV* phase map are acquired simultaneously, allowing a direct correlation between surface features and local electrical properties.

In practice, biases are applied to the sample while the tip is grounded for convenience. This is equivalent to the tip being biased relative to the sample as described above.

Table 1
Properties of the three probes used in this study. They are all made of silicon but coated with different materials. Tip radius and spring constant are nominal values. Both SCM-PIC-V2 [42] and DDESP-V2 [43] are the products of Bruker™ while AD-450-AS [44] is the product of Adama Innovations™.

Types	Coating materials	Tip radius	Spring constant
SCM-PIC-V2	Platinum-iridium	25 nm	0.10 N/m
DDESP-V2	Doped diamond	100 nm	80 N/m
AD-450-AS	Doped diamond	10 nm	450 N/m

2.2. Challenges of plan-view studies of HEMT structures

GaN-based HEMT structures are characterised by a 2DEG with a high carrier density near the surface. It is challenging to achieve plan-view SCM contrast in HEMT structures because the carrier density of the 2DEG is so high that standard imaging conditions for GaN, in which only an ac bias is applied [1], may not be sufficient to achieve carrier depletion [Fig. 1(b)]. Hence, in addition to the ac bias, a dc bias should also be applied to help deplete the 2DEG and thus achieve SCM contrast. Therefore, we need to develop techniques to facilitate accurate, convenient determination of the effective dc bias value.

Another challenge is that the contrast reported previously [32–34] is often weak and only with micron-scale resolution. One possible reason for the weak contrast could be the significant distance (e.g., typically >20 nm) between the conductive tip and the sub-surface 2DEG with no carriers in the intervening region (Fig. 1(b)). This means that the plates of the local capacitor are effectively further apart, reducing the capacitance signals and hence providing weak contrast. Therefore, the plan-view SCM contrast should be carefully optimised while maintaining a nanoscale resolution.

2.3. Scanning capacitance spectroscopy

The scanning capacitance spectroscopy (SCS) mode of SCM records local *dC/dV-V* curves at selected points on the sample surface.

In SCS mode, a tip is precisely positioned at a target position and contacts with it. As illustrated schematically in Fig. 2(a), a certain ac bias is additionally applied at a certain dc bias of the local *C-V* curve, so that the *dC/dV* amplitude value at this dc bias can be measured. This will contribute one data point to the local *dC/dV-V* curve. A complete *dC/dV-V* curve can be constructed if the ac bias sweeps the whole range of the dc biases. The *dC/dV-V* curve (Fig. 2(b)) is expected to be in the shape of a peak because it is the first derivative of the *C-V* curve (Fig. 2(a)). The peak position may indicate the effective dc bias that provides the strongest SCM contrast.

We explore the use of *dC/dV-V* curves in SCS mode to identify an appropriate dc bias for SCM imaging of HEMT structures.

3. Experimental

In this study, SCM was operated in an open-loop contact mode [1] using a Bruker Dimension Icon Pro AFM coupled with a Bruker SCM module. The measurements were taken at room temperature using a 90 kHz ac bias and a 990 MHz capacitance sensor. Three types of probes were tested for SCM characterisation of HEMT structures. Their nominal properties are listed in Table 1 for comparison.

The HEMT structure was grown on a Si (111) substrate by metal organic vapor-phase epitaxy (MOVPE). Its epitaxial structure is shown in

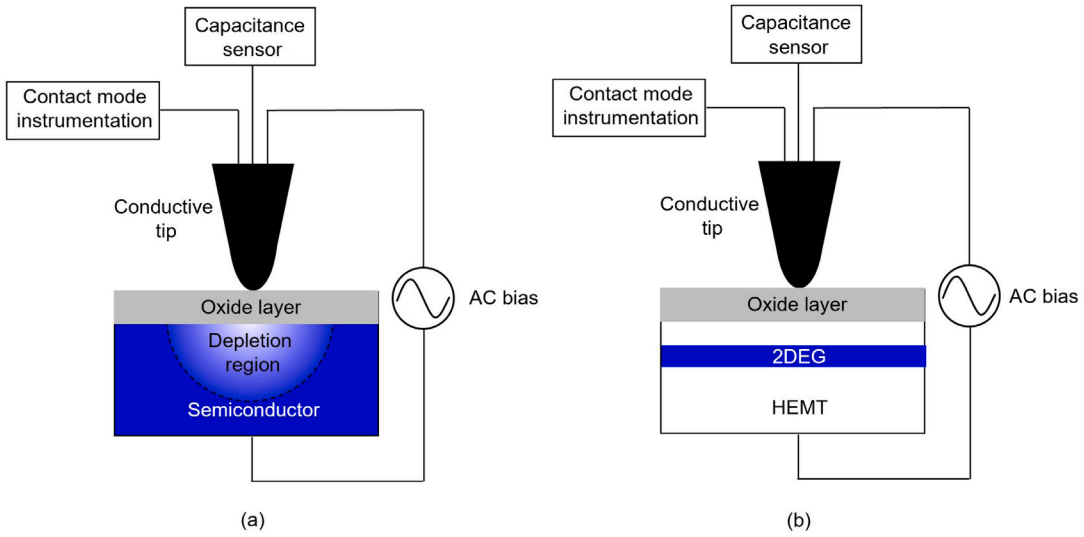

Fig. 1. Schematic of the formation of a nanoscale MOS capacitor by the conductive tip, oxide layer, and semiconductor sample in SCM: (a) in the case of an n-doped bulk semiconductor, a depletion region is modulated under the tip with an applied ac bias; (b) in the case of a HEMT structure, the 2DEG with high carrier density is difficult to deplete due to the insufficient ac bias in standard SCM setups. The intensity of the blue colour indicates the distribution of electrons. Based on [1].

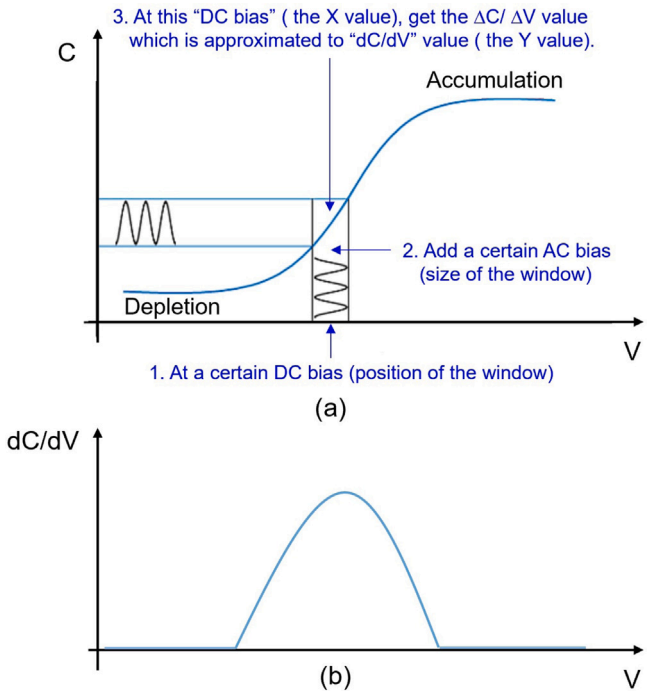

Fig. 2. (a) Principle of scanning capacitance spectroscopy mode in SCM, based on the *C-V* curve of an n-type semiconductor. The tip is biased while the sample is grounded. Adapted from Bruker SCM manual; (b) the corresponding *dC/dV-V* curve.

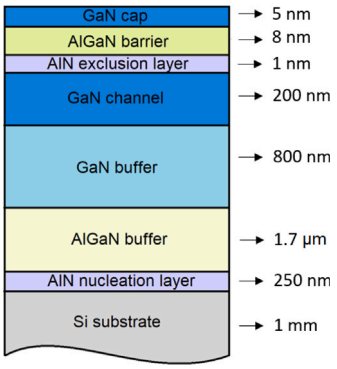

Fig. 3. Epitaxial structure of the HEMT sample.

Fig. 3. The buffer structure consists of a 1.7 μm thick compositionally-graded AlGaN layer and 800 nm thick GaN buffer layer on top of which were grown a GaN channel, an AlN exclusion layer, an AlGaN barrier, and a GaN cap with thicknesses of 200 nm, 1 nm, 8 nm and 5 nm respectively. All layers were unintentionally doped except the compositionally-graded AlGaN buffer layer which was iron doped. The Al ratio in the AlGaN buffer layer decreased gradually along the growth direction. Hall effect measurements at room temperature yield a sheet charge density of $1.12 \times 10^{13}\ \mathrm{cm}^{-2}$ and a mobility of $1.79 \times 10^{3}\ \mathrm{cm}^{2}\ \mathrm{V}^{-1}\ \mathrm{s}^{-1}$. The sample surface shows a low density of nanoscale fissures (Fig. 4) which have been previously reported in similar AlGaN/GaN heterostructures [39]. Our preliminary observations suggest that the fissures cause SCM contrast because the local structural changes alter the 2DEG properties. Here, we use the contrast generated by the fissures to optimise the plan-view SCM experimental procedure. We aim to address the underlying structure–property relationships in a later manuscript. To ensure a minimal resistance of the complete SCM circuit [Fig. 1], Ohmic contacts were fabricated on the sample surface by depositing Ti/Al/Ti/Au (15/50/20/100 nm) layers followed by rapid thermal annealing (RTA) at 710 °C. We note that Minj et al. [22] have also stressed the importance of using Ohmic contacts in SCM of GaN-based samples. However, our approach is distinct from that they use for cross-sectional SCM characterisation. Minj et al. [22] employ a back-contact. If this approach were used for GaN-on-Si HEMTs to conduct plan-view SCM characterisation, signals would be applied through the substrate, via unintentionally doped regions at the nitride-silicon interface [45] and across the highly resistive buffer region [23]. This would result in significant voltage drops, rendering the signal-to-noise ratio lower. Here, the Ohmic contacts were connected to the 2DEG directly, avoiding these additional resistances, and avoiding complications in data interpretation which may arise from applying a bias across multiple heterointerfaces.

The experimental setup for SCM characterisation of the HEMT test sample is shown in Fig. 5. The Ohmic contact of the sample was electrically connected to the steel disk using silver paste. Then, the

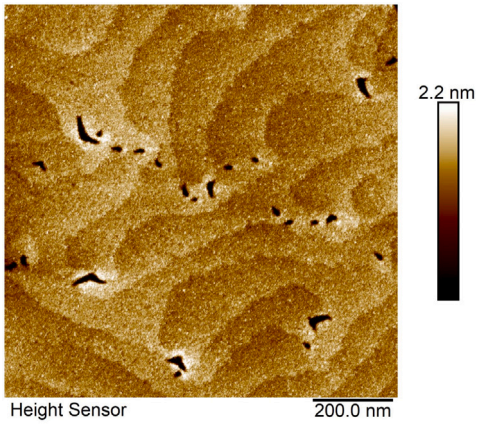

Fig. 4. Peak force AFM image of HEMT surface with fissures.

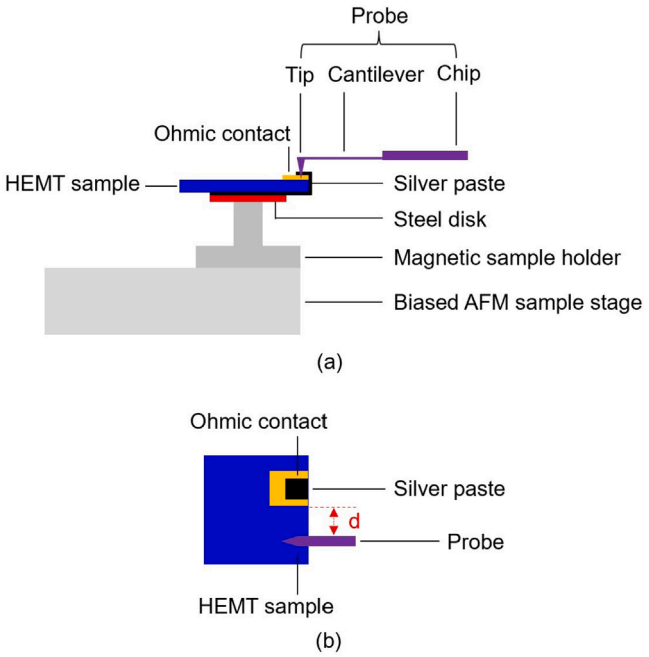

Fig. 5. Schematic of the experimental setup. (a) Side view and (b) top view.

magnetic sample holder connected the steel disk with the biased AFM sample stage. Biases were applied to the sample via the biased stage instead of to the tip, which was grounded. Hence, a low resistance electrical connection between the Ohmic contact of the sample and the biased sample stage is paramount to the experimental setup.

Prior to metallisation and the SCM characterisation, the same HEMT sample was characterised using a mercury probe capacitance-voltage measurement system from the Materials Development Corporation at the bias frequency of 10 kHz. The mercury probe was 766 μm in diameter. In contrast to the case in SCM, the mercury probe was biased while the sample was grounded.

4. Results and discussion

4.1. C-V and dC/dV-V curves of the HEMT structure

4.1.1. Mercury C-V curve

Fig. 6 shows a macroscopic *C-V* curve of the HEMT structure measured using the mercury probe. The sloping region only covers a narrow range of dc bias, which corresponds to a narrow peak in the

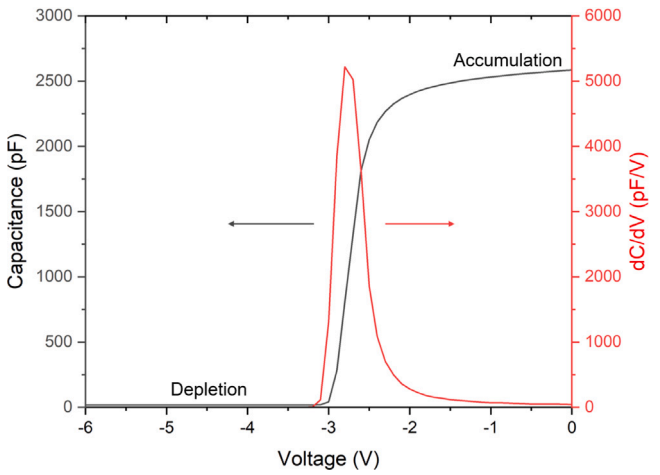

Fig. 6. Mercury *C-V* curve of the HEMT structure and its first derivative. The probe was biased while the sample was grounded.

dC/dV-V curve. Therefore, the effective dc bias range for SCM imaging is also expected to be narrow.

4.1.2. Comparison of dC/dV-V curves captured using different probes in SCS mode

SCM-PIC-V2 tip. We started with an SCM-PIC-V2 tip with the spring constant of 0.1 N/m which is a conventional choice for SCM characterisation of GaN [23,45–47].

Sumner [10] suggests that the tip should scan the edge of the sample to reduce the stray capacitance between the sample and the cantilever which may 'drown out' the desired SCM signals [Fig. 7]. To verify that, local SCS measurements at the same ac bias were conducted from the centre to the very edge of the HEMT sample of 1 cm × 1 cm in size. The overlapping area between the sample and the cantilever and hence the associated interstitial stray capacitance decreased as the tip was moved from the sample centre towards its edge. A continuous increase in the peak height in the *dC/dV-V* curves was observed [Fig. 8]. The curve labelled with 'edge' was collected at the furthest point just before the tip lost contact with the sample. The nominal length of the cantilever is 450 μm. When the tip was positioned on the sample surface at a distance of more than 450 μm from the sample edge, the metal-coated chip (see Fig. 5(a)) might also contribute to the stray capacitance.

Also, the distance *d* between the Ohmic contact and the tip position should be kept small to avoid a significant voltage drop between the contact and the tip position, otherwise it will not be possible to accurately estimate the bias at the tip position [Fig. 5(b)].

So, as a general rule, the tip should be positioned close to both the sample edge and the Ohmic contact so that strong *dC/dV-V* peaks can be achieved.

Regarding the SCM-PIC-V2 tip itself, although it has a chance to provide strong *dC/dV-V* peaks as shown, the repeatability is rather poor because the tip's spring constant is very small and hence the tip-sample contact is unstable at high biases. In particular, there may be local charging on the sample surface at high biases and hence a tip with a small spring constant may be easily repelled and lose contact with the surface intermittently. Additionally, the tip's metal coating can be easily worn with an increased tip electrical resistance and a blunt tip apex as result, especially when scanning hard materials like GaN in contact mode.

DDESP-V2 tip. Next, a DDESP-V2 tip with a hard diamond coating and large spring constant (80 N/m) was tested. It provides strong *dC/dV-V* peaks with good repeatability because the large spring constant of the tip allows for a stable tip-sample contact which is the key to electrical

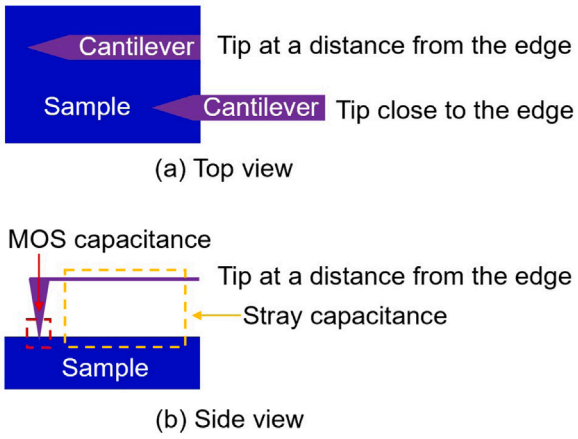

Fig. 7. (a) Two different scanning positions on the sample surface: at a large distance from the sample edge versus close to the edge; (b) When the tip is at a distance from the sample edge, stray capacitance between the cantilever and the sample is expected to be large. It may "drown out" the desired MOS capacitance signal between the tip and the sample. Based on [10].

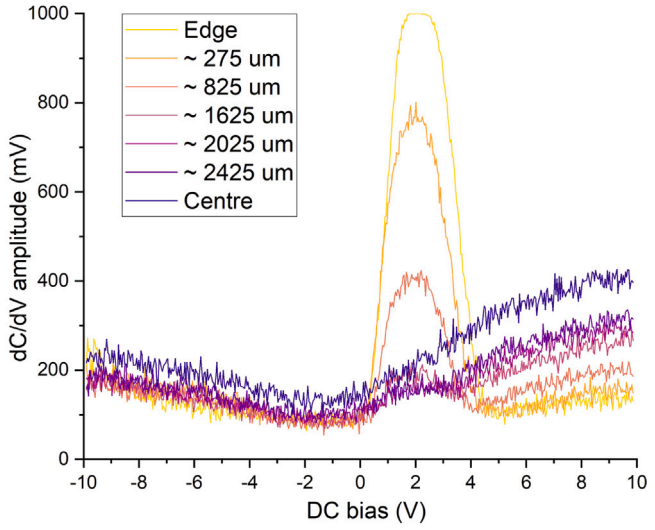

Fig. 8. Evolution of peaks in the local *dC/dV-V* curves recorded at different distances from the sample edge. SCM-PIC-V2 tip was used.

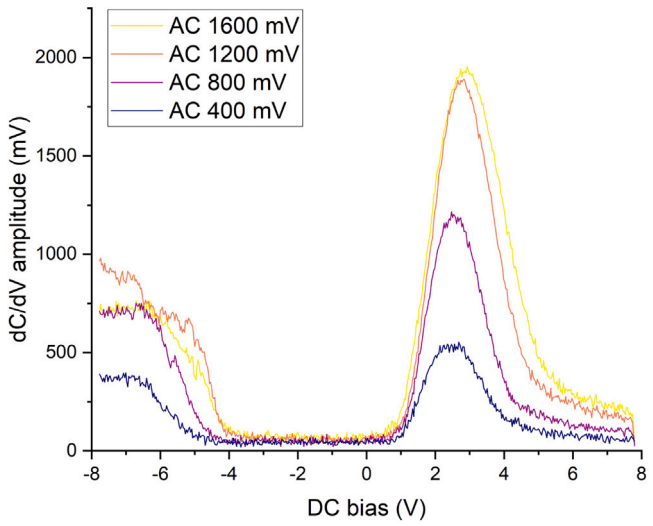

Fig. 9. Local *dC/dV-V* curves were recorded at different ac biases. DDESP-V2 tip was used.

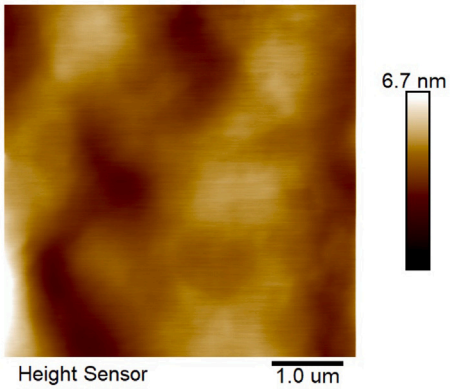

Fig. 10. Topography image of the HEMT structure surface with nanoscale fissures, captured using a DDESP-V2 tip.

characterisation. Also, the lifetime (i.e., the duration of the ability to capture electrical signals) of the tip is much longer.

The DDESP-V2 tip was used to investigate the impact of the ac bias on the *dC/dV-V* peak. Four different ac biases swept the same range of the dc biases. As shown in Fig. 9, the peak intensity increases as the ac bias is increased while the peak shift is insignificant.

Both Figs. 8 and 9 show that the peaks appear only within the positive dc bias range. Also, we note an increase in the dC/dV signal at larger negative sample biases in Fig. 9. At these biases we have observed in tunneling AFM (TUNA) experiments that current flows from tip to sample. We also observed damage to the sample surface in this regime (see Fig. S1 in the supplementary material). Data interpretation in this regime of the curve thus becomes difficult as the standard capacitor model is invalid in this regime and sample is damaged. Hence, in further optimisation of the SCM imaging conditions, we will only focus on the positive dc bias range.

However, the large DDESP-V2 tip radius (nominal tip radius: 100 nm) unfortunately prohibits SCM mapping at a nanoscale resolution (Fig. 10).

AD-450-AS tip. An AD-450-AS tip consists of a diamond-covered bulk silicon tip (Fig. 11). At the apex of the bulk tip is the sharp Adama diamond tip [48]. The tip is quite stiff with a spring constant of about 450 N/m. It combines all the desired properties to achieve *dC/dV-V* peaks (Fig. 12) with good repeatability, together with nanoscale resolution and a long lifetime. Although the *dC/dV-V* peak intensity is relatively low, it is sufficient to identify the peak position. The peak intensity is limited because the tip is sharp and robust, which means that the area of the local capacitor remains small. As a result, the capacitance signals are always weak.

The position of the peak given by the first derivative of the mercury *C-V* curve (Fig. 6) and that of the peaks in the SCS *dC/dV-V* curves (Figs. 8, 9, 12) are in close agreement. The reason for the opposite polarity is that the probe was biased in the mercury C-V measurement while the sample was biased in SCS. The different width of the *dC/dV-V* peaks observed in the two cases could be caused by the difference in electric field uniformity; the non-uniform field radiating from the small SCS tip is in contrast with the uniform field radiating from the relatively large mercury contact. Overall, SCS can help to identify an effective dc bias for the SCM imaging of HEMT structures through the *dC/dV-V* peaks.

The performance of the three probes is summarised in Table 2. Tables 1 and 2 together illustrate that a desired tip should be sharp, stiff, and coated with conductive hard material so that it can provide

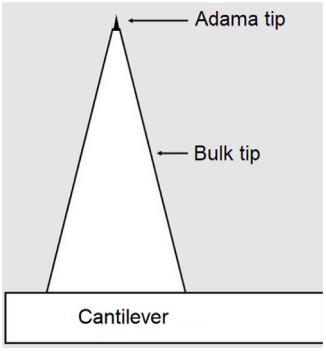

Fig. 11. Schematic structure of an AD-450-AS tip.
Source: Adapted from [48].

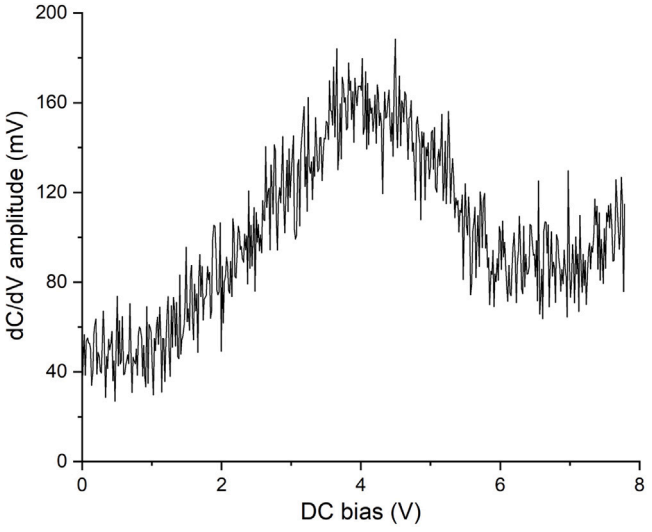

Fig. 12. A local *dC/dV-V* curve was recorded by using an AD-450-AS tip.

Table 2
Performance of the three probes used in SCS mode and SCM mode.

Types	Lifetime	Nano Resolution	SCS repeatability
SCM-PIC-V2	Short	Yes	Poor
DDESP-V2	Long	No	Good
AD-450-AS	Long	Yes	Good

nanoscale resolution, repeatable SCS *dC/dV-V* curves, and a long lifetime, which are difficult to achieve using the conventional metal-coated tips which are often employed in SCM of chemically doped samples. Based on our experiments, the diamond-coated AD-450-AS tip provides the best balance of characteristics among the tips trialed here. Hence, for the subsequent experiments, it is chosen for SCM imaging of the HEMT test structure.

4.2. Local dC/dV-V curves captured on and off fissures

For the SCS mode measurements, two areas of interest are defined: a measurement point on a fissure and another on a region without fissures (hereafter described as "off fissures") as marked in Fig. 13. The tip was precisely positioned on these two points on the sample surface (which was realised by using the "point and shoot" function in the Bruker Dimension Icon Pro AFM). The test conditions are the same for both points, with a 1.6 V ac bias sweeping the same positive range of the dc biases from 0 V to 8.2 V.

The resulting two *dC/dV-V* curves are shown in Fig. 14. To highlight the peaks, only the dc bias range from 1 V to 5 V is shown. The effective

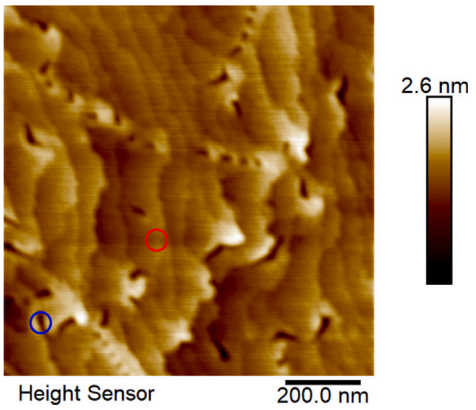

Fig. 13. One point on a fissure (highlighted in blue) and another point off fissures (highlighted in red) were tested in SCS mode.

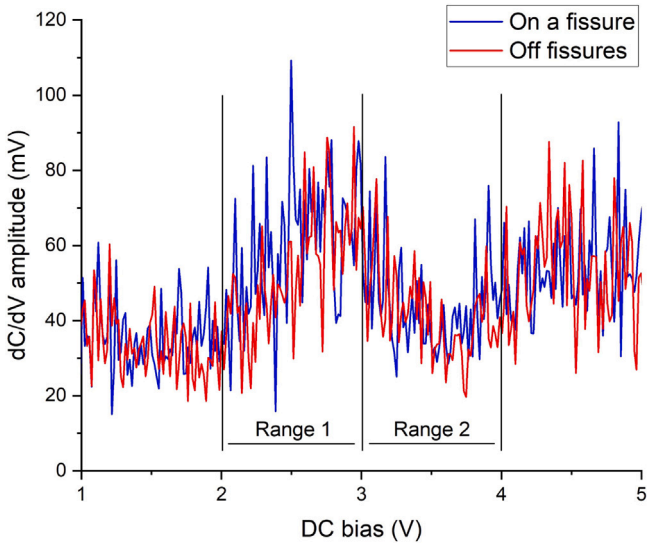

Fig. 14. Two *dC/dV-V* curves were captured on a fissure and off fissures on the HEMT surface in SCS mode.

dc bias for SCM imaging of this sample is expected to be in the dc bias range covered by the peaks (approximately 2–4 V). Hence, for the subsequent optimisation of the SCM contrast, different dc biases within that range were explored at a constant ac bias of 1.6 V.

4.3. Optimisation of the SCM contrast of the HEMT structure

4.3.1. Optimisation of dc bias

Optimisation of dc bias was divided into two ranges to cover the respective left and right flanks of the *dC/dV-V* peaks. In dc bias range 1 (2 to 3 V), five different and evenly distributed dc bias values (2.1, 2.3, 2.5, 2.7, and 2.9 V) were tested in the same scanned area in random order. The dc bias was varied for each 200 nm-wide horizontal section at a constant ac bias of 1.6 V. The same procedure was followed for exploring the optimum dc bias value in dc bias range 2 (3 to 4 V).

Fig. 15 shows the SCM results in dc bias range 1. Relatively good *dC/dV-V* amplitude contrast was observed at dc bias values of 2.7 and 2.9 V in which the areas with fissures show up as brighter than the areas off fissures. Only weak contrast was recorded at other dc bias values. Fig. 16 shows the SCM results in dc bias range 2. The areas with fissures show dark *dC/dV-V* amplitude contrast at dc bias values of 3.1, 3.3, 3.5, and 3.9 V except for 3.7 V.

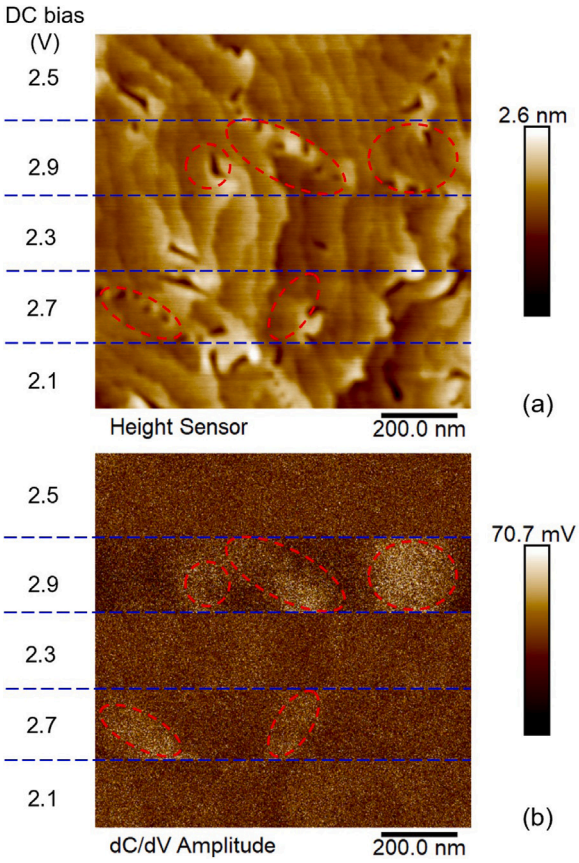

Fig. 15. (a) Topographical and (b) 0th-order flattened *dC/dV-V* amplitude data for an area on the HEMT surface. The ac bias value was kept constant at 1.6 V but the additional dc bias value varied from 2.1 V to 2.9 V when the tip was scanned in different stripes. Fissures show bright *dC/dV-V* amplitude contrast at dc bias values of 2.7 and 2.9 V as highlighted whilst the contrast is very weak at other dc bias values.

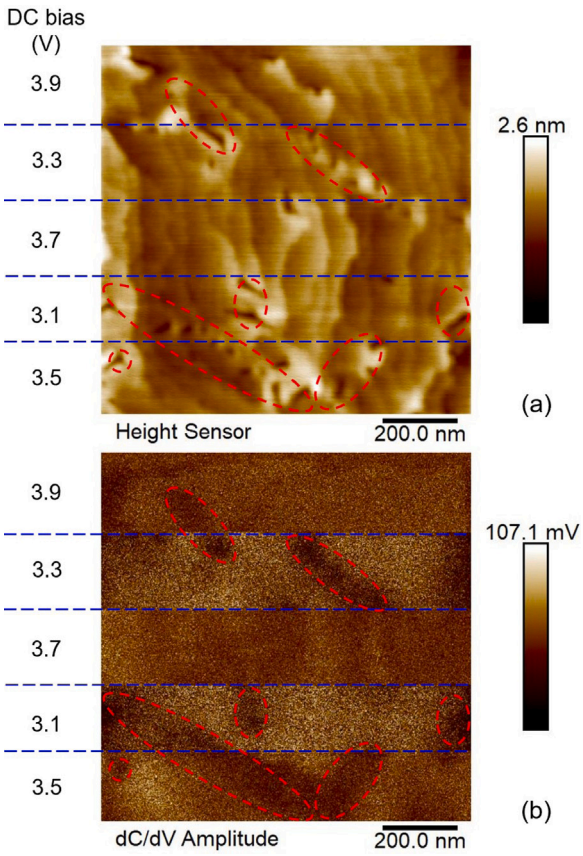

Fig. 16. (a) Topographical and (b) 0th-order flattened *dC/dV-V* amplitude data for the same area. The ac bias value was kept constant at 1.6 V but the additional dc bias value varied from 3.1 V to 3.9 V. Fissures show dark *dC/dV-V* amplitude contrast at dc bias values of 3.1, 3.3, 3.5, and 3.9 V as highlighted. 3.7 V provides a very weak contrast.

The dc bias optimisation procedure for this present sample indicates that a dc bias value of 2.9 V is best for a bright contrast for areas with fissures (Fig. 15) while a dc bias value of 3.3 V provides the strongest dark contrast for areas with fissures (Fig. 16). Fig. 17 compares the same sample surface scanned at the two optimised dc bias values, highlighting the contrast inversion between the two corresponding *dC/dV-V* amplitude images (Fig. 17(b) and (c)). We note that we are observing features with width as small as about 60 nm (Fig. 17(c)), consistent with our suggestion that the SCM resolution should be in the tens of nanometers regime.

In Fig. 17(b) and (c), almost all the fissures seen in the topographical image (Fig. 17(a)) show contrast, which suggests that fissures may have different local electrical properties from the surroundings.

The electrical properties of individual fissures may also differ from each other. Additionally, some non-fissure regions show similar (bright) contrast to the regions with fissures. This phenomenon may have different causes such as a sub-surface inhomogeneity of the AlGaN barrier layer thickness or alloy composition [32,33]. We aim to discuss the underlying structure–property relationships of the present sample in detail in a future manuscript.

It is important to note that observing a nanoscale feature such as a fissure exhibiting dark (or light) contrast in SCM is not diagnostic of its impact on the 2DEG, since whether it appears dark or light is sensitively dependent on the applied dc bias. These effects can only be understood in the context of bias-dependent imaging and/or SCS spectroscopy. The SCM contrast inversion reported in chemically doped samples is often said to be surface state related [49]. However, the mechanism of contrast inversion is different in samples with polarisation-induced doping like GaN-based HEMTs. To understand that, two hypothetical HEMT structures with different threshold voltages are taken as an example. A change in the threshold voltage (Fig. 18(a)) is expected to lead to a peak shift in the corresponding $dC/dV-V$ curve (Fig. 18(b)). Thus, the relative dC/dV amplitude relationship of them is just the opposite if they are probed at two different fixed dc bias values in both flanks of the peaks. As a result, the interpretation of the SCM contrast of GaN-based HEMTs is not straightforwardly related to carrier density as in chemically doped samples [1] but is influenced by shifts in threshold voltage.

4.3.2. Optimisation of ac bias

The impact of ac bias on SCM contrast of HEMT sample surface was also examined. The dc bias was fixed at the optimised value of 3.3 V while five different and evenly distributed ac bias values in the range around 1.6 V (1.0, 1.3, 1.6, 1.9, and 2.2 V) were tested for 200 nm-wide horizontal sections in random order. As shown in Fig. 19, ac bias has no significant impact on the SCM contrast as long as it exceeds the threshold value at which SCM contrast can be seen.

5. Comments

The relatively low signal-to-noise ratio of the SCM data collected with the sharp AD-450-AS tip is the result of a compromise between topographical nanoscale resolution (e.g., for fissures) and a low capacitance signal due to the small tip-sample contact area. Therefore, a high SCM contrast at a high topographical resolution cannot be achieved simultaneously on this sample with the current SCM module. However,

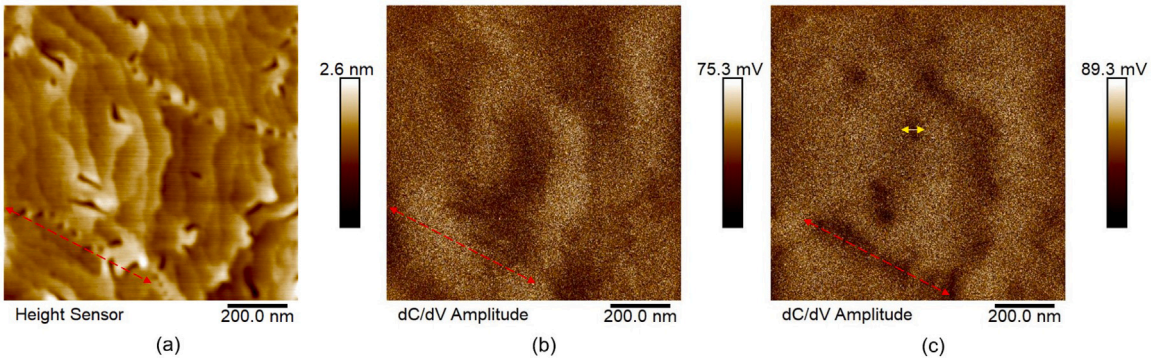

Fig. 17. (a) Topographical and (b), (c) *dC/dV-V* amplitude data for the same area. (a) and (b) were captured simultaneously at ac bias value of 1.6 V with dc bias value of 2.9 V while (c) was additionally captured at the same ac bias value but with different dc bias value of 3.3 V. Both (b) and (c) are 2nd-order flattened. The red lines are intended to indicate the same position, showing the sample drift between different scans. The yellow arrow in (c) highlights a feature with width as small as about 60 nm.

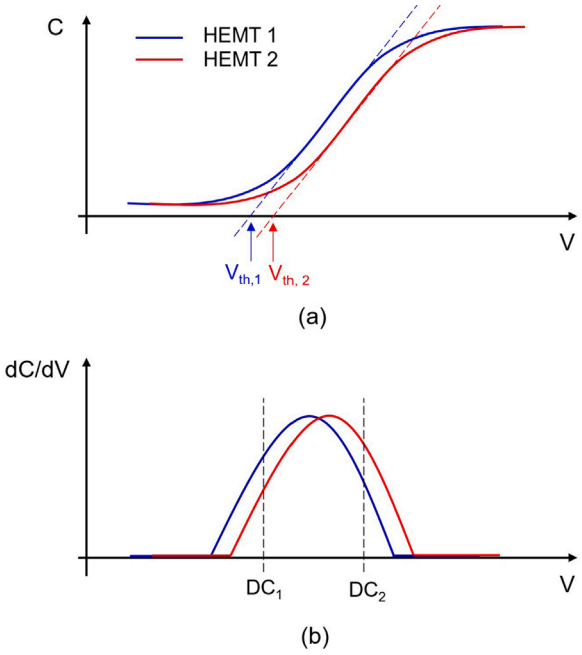

Fig. 18. Schematic drawing of the (a) $C-V$ and (b) $dC/dV-V$ curves of two hypothetical HEMTs with different threshold voltages $V_{th,1}$ and $V_{th,2}$.

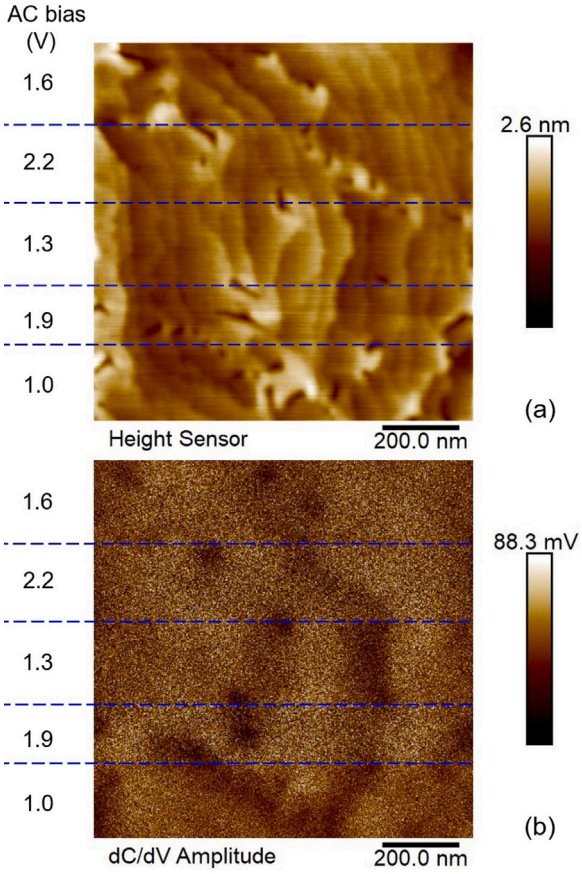

Fig. 19. (a) Topographical and (b) 2nd-order flattened *dC/dV-V* amplitude data for the same area. The dc bias was kept constant at 3.3 V while the ac bias varied from 1.0 V to 2.2 V when the tip was scanned in different stripes.

HEMT structures with thinner barriers may allow better signal to noise ratios, whilst in the general case, more sensitive detectors and the emerging scanning microwave impedance microscopy technology [50] may offer a solution to this dilemma.

Similar phenomena such as contrast inversion shown in this paper can also be seen when using other SCM tips. As an example, clear contrast inversion is shown by the DDESP-V2 tip in Fig. S2 in the supplementary information. Due to the poor spatial resolution related to the large tip radius, it is impossible to correlate the contrast with surface defects such as nanoscale fissures, but the global phenomenon is clearly shown.

Except for the characterisation of the surface features such as fissures, the methodology in this paper can also help us to use SCM to gain insights into the sub-surface features like inhomogeneities of the AlGaN barrier layer's thickness or composition in GaN-based HEMT structures [32,33]. These sub-surface features might not lead to identifiable surface topography. In that case, high topography resolution may not be necessary, and hence the decision on optimum tip type might be different. We might recommend the DDESP-V2 tip to get stronger SCM signals with the bigger tip-sample contact area in some cases.

6. Conclusion

The impact of the experimental setup and imaging conditions on the contrast observed in plan-view SCM characterisation of a HEMT structure with surface fissures has been investigated.

In terms of the experimental setup, the desired tip should be sharp enough to achieve nanoscale resolution. Its coating should be made of conductive hard material to have a long lifetime. The key point is that it should have a large spring constant to provide a stable tip-sample contact and hence repeatable SCS and SCM signals. The selected tip should be positioned close to both the sample edge and Ohmic contact to enhance both SCS and SCM signals.

In terms of the imaging conditions, this study shows that, in addition to the ac bias, a dc bias should be applied to help deplete the 2DEG of the HEMT structure and hence achieve SCM contrast. The local *dC/dV-V* curves provided by the SCS mode indicate the approximate range of the effective dc bias values. The further optimisation of the dc bias can eventually determine two optimised dc bias values which can provide the strongest SCM contrast. Contrast inversion is observed between them. It was experimentally demonstrated that the dc bias has a significant impact on the SCM contrast while the ac bias value is less important, provided the latter exceeds a certain threshold value.

This study provides a solid basis for studies into the structure–property relationships in GaN-based HEMT structures. The impact of fissures, dislocations and inhomogeneities in barrier on threshold voltage will be the subject of future studies. The methodology could potentially also be applied to other types of HEMT structures such as GaAs-based HEMT structures, and other highly-doped samples.

Declaration of competing interest

The authors declare that they have no known competing financial interests or personal relationships that could have appeared to influence the work reported in this paper.

Data availability

The data that support the findings of this study are openly available at the following URL/DOI: https://doi.org/10.17863/CAM.100633

Acknowledgements

The authors would like to thank Dr Peter De Wolf and Dr Vishal Panchal from Bruker Nano Surfaces & Metrology for fruitful discussions and support. C. Chen would like to thank China Scholarship Council, China and Cambridge Commonwealth, European & International Trust, United Kingdom for a CSC Cambridge Scholarship. Materials studied here were grown using the EPSRC National Epitaxy Facility, United Kingdom under EPSRC Grant EP/N017927/1. The access to the AFM was supported under Cambridge Royce facilities, United Kingdom grant EP/P024947/1 and Sir Henry Royce Institute, United Kingdom recurrent grant EP/R00661X/1.

Appendix A. Supplementary data

Supplementary material related to this article can be found online at https://doi.org/10.1016/j.ultramic.2023.113833.

References

[1] R.A. Oliver, Advances in AFM for the electrical characterization of semiconductors, Rep. Progr. Phys. 71 (7) (2008) 076501.
[2] G.H. Buh, H.J. Chung, J.H. Yi, I.T. Yoon, Y. Kuk, Electrical characterization of an operating Si pn-junction diode with scanning capacitance microscopy and Kelvin probe force microscopy, J. Appl. Phys. 90 (1) (2001) 443–448.
[3] F. Giannazzo, D. Goghero, V. Raineri, S. Mirabella, F. Priolo, Scanning capacitance microscopy on ultranarrow doping profiles in Si, Appl. Phys. Lett. 83 (13) (2003) 2659–2661.
[4] K.M. Wong, Study of the electronic structure of individual free-standing Germanium nanodots using spectroscopic scanning capacitance microscopy, Japan. J. Appl. Phys. 48 (8R) (2009) 085002.
[5] S. Zhang, Y. Lv, Z. Jiang, X. Yang, Electrical properties of individual self-assembled GeSi quantum rings, J. Appl. Phys. 110 (9) (2011) 094313.
[6] Y. Lv, J. Cui, Z.M. Jiang, X. Yang, Nanoscale electrical property studies of individual GeSi quantum rings by conductive scanning probe microscopy, Nanoscale Res. Lett. 7 (1) (2012) 1–6.
[7] J. Smoliner, W. Brezna, P. Klang, A.M. Andrews, G. Strasser, Quantitative scanning capacitance microscopy on single subsurface InAs quantum dots, Appl. Phys. Lett. 92 (9) (2008) 092112.
[8] A. Szyszka, W. Dawidowski, A. Stafiniak, J. Prażmowska, B. Ściana, M. Tłaczała, A cross-sectional scanning capacitance microscopy characterization of GaAs based solar cell structures, Cryst. Res. Technol. 52 (6) (2017) 1700019.
[9] P.J. Hansen, Y.E. Strausser, A.N. Erickson, E.J. Tarsa, P. Kozodoy, E.G. Brazel, J.P. Ibbetson, U. Mishra, V. Narayanamurti, S.P. DenBaars, et al., Scanning capacitance microscopy imaging of threading dislocations in GaN films grown on (0001) sapphire by metalorganic chemical vapor deposition, Appl. Phys. Lett. 72 (18) (1998) 2247–2249.
[10] J. Sumner, Scanning probe microscopy studies on gallium nitride (Ph.D. thesis), University of Cambridge, 2008.
[11] F. Bassani, P. Periwal, B. Salem, N. Chevalier, D. Mariolle, G. Audoit, P. Gentile, T. Baron, Dopant profiling in silicon nanowires measured by scanning capacitance microscopy, Phys. Status Solidi (RRL)–Rapid Res. Lett. 8 (4) (2014) 312–316.
[12] L. Wang, S. Guillemin, J.-M. Chauveau, V. Sallet, F. Jomard, R. Brenier, V. Consonni, G. Brémond, Characterization of carrier concentration in ZnO nanowires by scanning capacitance microscopy, Phys. Status Solidi (c) 13 (7–9) (2016) 576–580.
[13] K. Maknys, O. Douhéret, S. Anand, Electrical characterization of InGaAs/InP quantum wells by scanning capacitance microscopy, Appl. Phys. Lett. 83 (20) (2003) 4205–4207.
[14] U.K. Mishra, P. Parikh, Y.-F. Wu, Algan/gan HEMTs-an overview of device operation and applications, Proc. IEEE 90 (6) (2002) 1022–1031.
[15] I. Khalil, A. Liero, M. Rudolph, R. Lossy, W. Heinrich, GaN HEMT potential for low-noise highly linear RF applications, IEEE Microw. Wirel. Compon. Lett. 18 (9) (2008) 605–607.
[16] N. Ikeda, Y. Niiyama, H. Kambayashi, Y. Sato, T. Nomura, S. Kato, S. Yoshida, GaN power transistors on Si substrates for switching applications, Proc. IEEE 98 (7) (2010) 1151–1161.
[17] H. Amano, Y. Baines, E. Beam, M. Borga, T. Bouchet, P.R. Chalker, M. Charles, K.J. Chen, N. Chowdhury, R. Chu, et al., The 2018 GaN power electronics roadmap, J. Phys. D: Appl. Phys. 51 (16) (2018) 163001.
[18] H. Jia, L. Guo, W. Wang, H. Chen, Recent progress in GaN-based light-emitting diodes, Adv. Mater. 21 (45) (2009) 4641–4646.
[19] A.F. Jarjour, R.A. Taylor, R.A. Oliver, M.J. Kappers, C.J. Humphreys, A. Tahraoui, Cavity-enhanced blue single-photon emission from a single InGaN/GaN quantum dot, Appl. Phys. Lett. 91 (5) (2007) 052101.
[20] R.A. Oliver, F.C.P. Massabuau, M.J. Kappers, W.A. Phillips, E.J. Thrush, C.C. Tartan, W.E. Blenkhorn, T.J. Badcock, P. Dawson, M.A. Hopkins, et al., The impact of gross well width fluctuations on the efficiency of GaN-based light emitting diodes, Appl. Phys. Lett. 103 (14) (2013) 141114.
[21] F.C.P. Massabuau, M.J. Davies, F. Oehler, S.K. Pamenter, E.J. Thrush, M.J. Kappers, A. Kovacs, T. Williams, M.A. Hopkins, C.J. Humphreys, et al., The impact of trench defects in InGaN/GaN light emitting diodes and implications for the "green gap" problem, Appl. Phys. Lett. 105 (11) (2014) 112110.
[22] A. Minj, M. Zhao, B. Bakeroot, K. Paredis, Imaging confined and bulk p-type/n-type carriers in (Al, Ga) N heterostructures with multiple quantum wells, Appl. Phys. Lett. 118 (3) (2021) 032104.
[23] F.S. Choi, J.T. Griffiths, C. Ren, K.B. Lee, Z.H. Zaidi, P.A. Houston, I. Guiney, C.J. Humphreys, R.A. Oliver, D.J. Wallis, Vertical leakage mechanism in GaN on Si high electron mobility transistor buffer layers, J. Appl. Phys. 124 (5) (2018) 055702.
[24] D. Zhu, D.J. Wallis, C.J. Humphreys, Prospects of III-nitride optoelectronics grown on si, Rep. Progr. Phys. 76 (10) (2013) 106501.
[25] N. Mohan, Manikant, R. Soman, S. Raghavan, Integrating AlGaN/GaN high electron mobility transistor with Si: A comparative study of integration schemes, J. Appl. Phys. 118 (13) (2015) 135302.
[26] Y. Sugawara, Y. Ishikawa, A. Watanabe, M. Miyoshi, T. Egawa, Characterization of dislocations in GaN layer grown on 4-inch Si (111) with AlGaN/AlN strained layer superlattices, Japan. J. Appl. Phys. 55 (5S) (2016) 05FB08.
[27] B. Heying, E.J. Tarsa, C.R. Elsass, P. Fini, S.P. DenBaars, J.S. Speck, Dislocation mediated surface morphology of GaN, J. Appl. Phys. 85 (9) (1999) 6470–6476.
[28] S. Besendörfer, E. Meissner, F. Medjdoub, J. Derluyn, J. Friedrich, T. Erlbacher, The impact of dislocations on AlGaN/GaN Schottky diodes and on gate failure of high electron mobility transistors, Sci. Rep. 10 (1) (2020) 1–12.
[29] M. Wohlfahrt, M.J. Uren, Y. Yin, K.B. Lee, M. Kuball, Vertical field inhomogeneity associated with threading dislocations in GaN high electron mobility transistor epitaxial stacks, Appl. Phys. Lett. 119 (24) (2021) 243502.
[30] S. Arulkumaran, T. Egawa, H. Ishikawa, T. Jimbo, Comparative study of drain-current collapse in AlGaN/GaN high-electron-mobility transistors on sapphire and semi-insulating SiC, Appl. Phys. Lett. 81 (16) (2002) 3073–3075.
[31] S. Ghosh, S.M. Dinara, P. Mukhopadhyay, S.K. Jana, A. Bag, A. Chakraborty, E.Y. Chang, S. Kabi, D. Biswas, Effects of threading dislocations on drain current dispersion and slow transients in unpassivated AlGaN/GaN/Si heterostructure field-effect transistors, Appl. Phys. Lett. 105 (7) (2014) 073502.

[32] K.V. Smith, E.T. Yu, J.M. Redwing, K.S. Boutros, Scanning capacitance microscopy of AlGaN/GaN heterostructure field-effect transistor epitaxial layer structures, Appl. Phys. Lett. 75 (15) (1999) 2250–2252.
[33] K.V. Smith, E.T. Yu, J.M. Redwing, K.S. Boutros, Local electronic properties of AlGaN/GaN heterostructures probed by scanning capacitance microscopy, J. Electron. Mater. 29 (3) (2000) 274–280.
[34] K.V. Smith, X.Z. Dang, E.T. Yu, J.M. Redwing, Charging effects in AlGaN/GaN heterostructures probed using scanning capacitance microscopy, J. Vac. Sci. Technol. B 18 (4) (2000) 2304–2308.
[35] C. Williams, J. Slinkman, W. Hough, H. Wickramasinghe, Lateral dopant profiling with 200 nm resolution by scanning capacitance microscopy, Appl. Phys. Lett. 55 (16) (1989) 1662–1664.
[36] C. Williams, J. Slinkman, W. Hough, H. Wickramasinghe, Lateral dopant profiling on a 100 nm scale by scanning capacitance microscopy, J. Vac. Sci. Technol. A 8 (2) (1990) 895–898.
[37] A. Erickson, L. Sadwick, G. Neubauer, J. Kopanski, D. Adderton, M. Rogers, Quantitative scanning capacitance microscopy analysis of two-dimensional dopant concentrations at nanoscale dimensions, J. Electr. Mater. 25 (1996) 301–304.
[38] V. Zavyalov, J. McMurray, C. Williams, Advances in experimental technique for quantitative two-dimensional dopant profiling by scanning capacitance microscopy, Rev. Sci. Instrum. 70 (1) (1999) 158–164.
[39] M.D. Smith, D. Thomson, V.Z. Zubialevich, H. Li, G. Naresh-Kumar, C. Trager-Cowan, P.J. Parbrook, Nanoscale fissure formation in AlxGa1–xN/GaN heterostructures and their influence on Ohmic contact formation, Phys. Status Solidi (a) 214 (1) (2017) 1600353.
[40] C.C. Williams, Two-dimensional dopant profiling by scanning capacitance microscopy, Annu. Rev. Mater. Sci. 29 (1) (1999) 471–504.
[41] C. Eckhardt, W. Brezna, O. Bethge, E. Bertagnolli, J. Smoliner, Tip geometry effects in scanning capacitance microscopy on GaAs Schottky and metal-oxide-semiconductor-type junctions, J. Appl. Phys. 105 (11) (2009) 113709.
[42] Bruker, SCM-PIC-V2, [Online; accessed 19-August-2022], https://www.brukerafmprobes.com/p-3951-scm-pic-v2.aspx.
[43] Bruker, DDESP-V2, [Online; accessed 19-August-2022], https://www.brukerafmprobes.com/p-3884-ddesp-v2.aspx.
[44] Adama, APEX SHARP, [Online; accessed 19-August-2022], https://www.adama.tips/products-apex-sharp.
[45] S. Ghosh, A. Hinz, S.M. Fairclough, B.F. Spiridon, A. Eblabla, M.A. Casbon, M.J. Kappers, K. Elgaid, S. Alam, R.A. Oliver, et al., Origin (s) of anomalous substrate conduction in MOVPE-Grown GaN HEMTs on highly resistive silicon, ACS Appl. Electr. Mater. 3 (2) (2021) 813–824.
[46] J. Sumner, R.A. Oliver, M.J. Kappers, C.J. Humphreys, Scanning capacitance microscopy studies of unintentional doping in epitaxial lateral overgrowth GaN, J. Appl. Phys. 106 (10) (2009) 104503.
[47] M.J. Kappers, T. Zhu, S.L. Sahonta, C.J. Humphreys, R.A. Oliver, SCM and SIMS investigations of unintentional doping in III-nitrides, Phys. Status Solidi c 12 (4–5) (2015) 403–407.
[48] Adama, Products, [Online; accessed 21-August-2022], https://www.adama.tips/products.
[49] R. Stephenson, A. Verhulst, P. De Wolf, M. Caymax, W. Vandervorst, Contrast reversal in scanning capacitance microscopy imaging, Appl. Phys. Lett. 73 (18) (1998) 2597–2599.
[50] M.E. Barber, E.Y. Ma, Z.-X. Shen, Microwave impedance microscopy and its application to quantum materials, Nat. Rev. Phys. 4 (1) (2022) 61–74.